The Journal of Chemical Physics

RESEARCH ARTICLE | MARCH 15 2021

^{2}H NMR study on temperature-dependent water dynamics in amino-acid functionalized silica nanopores

Special Collection: Fluids in Nanopores

Elisa Steinrücken ; Till Wissel; Martin Brodrecht ; Hergen Breitzke; Julia Regentin; Gerd Buntkowsky ; Michael Vogel

J. Chem. Phys. 154, 114702 (2021)
https://doi.org/10.1063/5.0044141

The Journal of Chemical Physics ARTICLE scitation.org/journal/jcp

^{2}H NMR study on temperature-dependent water dynamics in amino-acid functionalized silica nanopores

Cite as: J. Chem. Phys. 154, 114702 (2021); doi: 10.1063/5.0044141
Submitted: 14 January 2021 • Accepted: 25 February 2021 •
Published Online: 15 March 2021

Elisa Steinrücken,[1] Till Wissel,[2] Martin Brodrecht,[2] Hergen Breitzke,[2] Julia Regentin,[1] Gerd Buntkowsky,[2] and Michael Vogel[1,a)]

AFFILIATIONS

[1]Institute for Condensed Matter Physics, Technische Universität Darmstadt, Hochschulstr. 6, 64289 Darmstadt, Germany
[2]Eduard-Zintl-Institut für Anorganische und Physikalische Chemie, Technische Universität Darmstadt, Alarich-Weiss-Str. 8, 64287 Darmstadt, Germany

Note: This paper is part of the JCP Special Topic on Fluids in Nanopores.
[a)]**Author to whom correspondence should be addressed:** michael.vogel@physik.tu-darmstadt.de

ABSTRACT

We prepare various amino-acid functionalized silica pores with diameters of ~6 nm and study the temperature-dependent reorientation dynamics of water in these confinements. Specifically, we link basic Lys, neutral Ala, and acidic Glu to the inner surfaces and combine ^{2}H nuclear magnetic resonance spin–lattice relaxation and line shape analyses to disentangle the rotational motions of the surfaces groups and the crystalline and liquid water fractions coexisting below partial freezing. Unlike the crystalline phase, the liquid phase shows reorientation dynamics, which strongly depends on the chemistry of the inner surfaces. The water reorientation is slowest for the Lys functionalization, followed by Ala and Glu and, finally, the native silica pores. In total, the rotational correlation times of water at the different surfaces vary by about two orders of magnitude, where this span is largely independent of the temperature in the range ~200–250 K.

I. INTRODUCTION

In many natural and technological environments, water exists in nanoscopic confinements. Therefore, a detailed knowledge about the dynamics of water under such severe geometrical restraints is key to understanding biological functions or geological and technological processes.[1,2] Owing to this far-reaching significance, a large body of scientific studies focused on the dynamical behaviors of confined waters and gathered a wealth of information.[3–7] It was reported that interfaces interrupt the hydrogen-bond network, resulting in many exotic features, which are not found in the bulk.[7] Many researchers investigated the fast dynamics of confined water at room temperature.[8–11] A generally observed slowdown of interfacial water was regarded as largely independent of the chemical nature and overall geometry of the interface[10] or as significantly affected by the type of the surface groups.[12] Other scientists used the freezing-point depression in confinement[13,14] to explore the supercooled state of water,[15–23] which is generally assumed to be of fundamental importance for the anomalies of the liquid.[24,25] While the dynamics of cooled water in various confinements share a number of common properties, there are also features, which differ in soft and hard environments.[21–23] Overall, the dependence of water dynamics on the properties of the confinement is still elusive.

In biological circumstances, hydration shells are intricately related with macromolecular motions. In particular, the water motions around proteins are essential for the flexibility and functions of these biomolecules.[26–30] Apart from many studies under ambient conditions,[7,11,31] various experimental methods were employed to ascertain water dynamics in dependence on the protein structure and the hydration level in broad temperature and dynamic ranges, including neutron scattering,[32–35] broadband dielectric spectroscopy (BDS),[36–41] and nuclear magnetic resonance (NMR)

experiments.[42–46] Furthermore, molecular dynamics simulations proved to be a very powerful tool to investigate water–protein dynamical couplings.[3,12,47–50] It was found that the chemical and geometrical diversity of protein surfaces leads to a strong heterogeneity of water dynamics in the hydration shell.[12,50] Not least because of this diversity, the feedback loop between water and protein motions remains incompletely understood. Since experimental approaches struggle to discriminate between water dynamics at different amino acids, it was recently proposed to reduce the heterogeneity and resort to homopolypeptide solutions for a basic understanding.[51,52]

Other dynamical studies confined water to mesoporous silica MCM-41 and SBA-15.[16,53–55] These materials feature hexagonally ordered pore arrays with a high surface area and a good thermal stability, whereat the pores have a defined cylindrical shape with a tunable pore diameter in the nanometer range. Moreover, their inner surfaces and, thus, their hydrogen-bonding properties can be modified by controlled chemical functionalization.[56] The available control over the pore geometry enabled insight into the dependence of water dynamics on the confinement size.[57–64] Likewise, the possibility of surface modification provided information about the role of guest–host interactions.[65–68] In addition, functionalized mesoporous silica have important applications, e.g., in heterogeneous catalysis[69] or for drug delivery.[70]

The dynamical behaviors of confined waters are particularly complex when partial crystallization occurs at high hydration levels or large pore diameters.[71] Under such circumstances, non-freezable water near the macromolecular surfaces or pore walls coexists with freezable water in the central regions of the confinements. Thus, a liquid water fraction is sandwiched between the confining matrix and an ice core below the melting point T_m, which depends on the confinement size according to the Gibbs–Thomson relation.[13,14,66] The liquid water undergoes a glass transition upon further cooling, while the ice core may show different structures and faster dynamics as compared to hexagonal bulk ice, which can additionally be present in studies on porous materials when excess water freezes outside the pore volumes. Thus, between T_m and the glass transition temperature T_g, three dynamically distinguishable water fractions can coexist in confinement studies: confined liquid, confined crystal, and external ice.

Here, we functionalize mesoporous silica with amino acids to generate well defined biomimetic confinements. In detail, we bind alanine (Ala), glutamic acid (Glu), or lysine (Lys) to the inner silica surfaces. In doing so, 3-(aminopropyl)triethoxysilane (APTES) serves as the linker between the silanol groups and the amino acids. In this way, we change not only the charge of the inner surfaces but also the flexibility of the functional groups because Ala has a neutral methyl group as the residue, while Glu and Lys have residues comprising three or four carbon atoms with an acidic and basic end group, respectively. For comparison, we also study the water dynamics in silica pores modified by the mere APTES linkers and we compare our findings with the previous results for native SBA-15 silica.[62] Despite the different functional groups, all studied host materials still exhibit similar pore diameters of ~6 nm. Thus, these materials are well suited to study changes in water dynamics mediated through the interaction with specific amino acids.

Moreover, we exploit that ^{2}H NMR proved to be a versatile tool to characterize the rotational dynamics of D_2O confined to silica[18,72,73] or protein[74–76] matrices. As a result of chemical exchange, the deuterons of the present samples are, however, distributed between not only the liquid and crystalline water fractions but also the amide and amine groups of the framework. Therefore, we combine spin–lattice relaxation (SLR) with line shape analysis (LSA) to disentangle the signals from the respective deuteron species and to ascertain their dynamics in a broad temperature range. Furthermore, we compare the obtained rotational correlation times with those for water in the bulk liquid, in the native pores, and in an amino-acid solution. In this way, we determine the dependence of water reorientation on the chemistry of inner surfaces.

II. PREPARATION OF AMINO-ACID FUNCTIONALIZED MESOPOROUS SILICA

The coupling of amino acids to SBA-15 silica was established in previous work.[77] We use this protocol to prepare mesoporous silica functionalized with neutral Ala, acidic Glu, or basic Lys. In the cases of Glu and Lys, there is an excess of carboxyl groups and amino groups, which are deprotonated and protonated in a basically neutral aqueous environment, respectively. Therefore, Glu functionalization results in more negative surface charge than Lys functionalization, while Ala takes an intermediate position.

The synthesis protocol involves SBA-15 silica modified with APTES linkers as the starting material. The preparation and characterization of this starting material was described in detail in a previous study.[78] It will be denoted as SBA–APT in the following.[79] Figure 1 illustrates the used synthetic routes to functionalize SBA–APT with the chosen amino acids. Like in solid-phase peptide

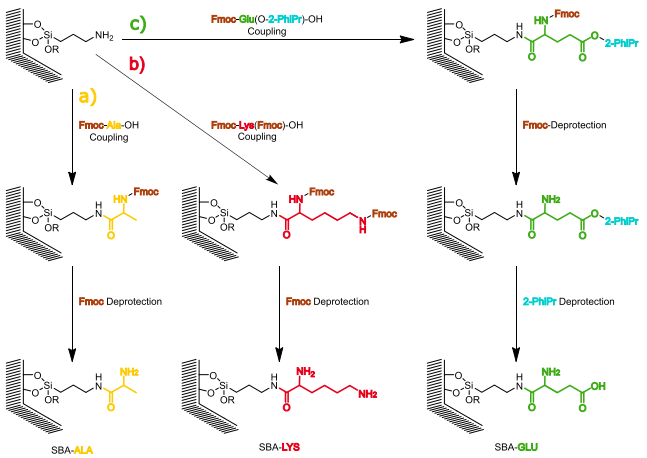

FIG. 1. Synthesis scheme for the different functionalizations of the SBA–APT starting material. Route (a) shows the coupling of Fmoc-Ala-OH and the cleavage of the Fmoc protective group to obtain the desired product SBA–ALA. In route (b), the approach to synthesize SBA–LYS is shown. It starts with the coupling of Fmoc-Lys(Fmoc)-OH and is terminated by the secession of the Fmoc protection groups. In route (c), SBA–APT is functionalized with Fmoc-Glu(2-PhiPr)-OH, and then, first the Fmoc protection group and then the 2-PhiPr protection group are removed to obtain SBA–GLU. Fmoc = fluorenylmethoxycarbonyl and 2-PhiPr = 2-phenylisopropyl ester.

synthesis, the general challenge in this endeavor is the protecting group strategy. Specifically, it must be ensured that carboxyl and amine groups, which are not supposed to react, are protected so that a defined monolayer of amino acids is formed. Appropriate protective groups withstand the reaction conditions during the coupling and can readily be cleaved off after the reaction under conditions, which are as mild as possible to avoid damage of the pore architecture and the preceding functionalization by the cleavage solution. We protect the amine groups of the amino acids by fluorenylmethoxycarbonyl (Fmoc) groups. These can be cleaved efficiently by a 20 vol. solution of piperidine in dimethylformamide (DMF) at room temperature without altering the silica material.[77] This strategy allows us to implement routes (a) and (b), which enable Ala and Lys functionalizations, respectively. In route (c), in addition to the Fmoc group, another protecting group must be used for the second carboxyl group of Glu. We choose 2-phenylisopropyl ester (2-PhiPr), which can be detached efficiently utilizing a 2 vol. % trifluoroacetic acid (TFA) in dichloromethane (DCM) solution at room temperature[80–82] while maintaining the pore architecture. We will refer to the SBA-15 materials thus functionalized with Ala, Lys, or Glu as SBA–ALA, SBA–LYS, and SBA–GLU, respectively.

A. Details of the synthesis

1. General

The chemicals were purchased from Carl Roth, Sigma-Aldrich, and Novabiochem. They were used without purification unless explicitly mentioned.

2. Starting material

The synthesis of SBA–APT was described in previous work.[77] The starting material for the present synthesis was taken from a batch, which was characterized and used in a recent study on confined LiCl aqueous solutions.[78]

3. Amino acid coupling

For the coupling of the amino acids, we dissolved 784.6 mg (2.06 mmol, 1.97 equiv.) of 1-[bis(dimethylamino)methylene]-1H-1,2,3-triazolo[4,5-b]pyridinium 3-oxide hexafluorophosphate and 2.1 mmol (2 equiv.) of the respective amino acid in 10 ml DMF. By adding 729 μl (4.19 mmol, 4 equiv.) of *N*-ethyl-*N*-(propan-2-yl)propan-2-amine to the solution and shaking for 2 min, the carboxyl group of the amino acid was activated. 500 mg (1.05 mmol NH_2 linker, 1 equiv.) of dried SBA–APT were added to the yellow solution and the suspension was shaken for 18 h at 1200 rpm and room temperature. The resulting solid was filtered off and washed three times with each DMF and deionized water and one time with ethanol. The obtained product was predried under air flow and completely dried under reduced pressure at room temperature.

4. Deprotection of the Fmoc group

A suspension of the resulting amino acid functionalized carrier material in 10 ml of a 20 vol. % piperidine in DMF solution was shaken for 16 h at 1200 rpm and room temperature. The solid was filtered off and washed three times with each DMF and deionized water and one time with ethanol. The product was predried under air flow and completely dried under reduced pressure at room temperature.

5. Deprotection of the 2-PhiPr group

The amino acid functionalized carrier material was shaken at 1200 rpm and room temperature for 16 h in 10 ml of a 2 vol. % TFA in DCM solution. The solid was filtered off and washed three times with each DCM and deionized water and one time with ethanol. The product was predried under air flow and completely dried under reduced pressure at room temperature. The remaining TFA inside the pores was washed off by shaking the solid three times for 1 h in 30 ml of a 50 mM hydrochloric acid solution. The product was then washed with deionized water until the eluent had a neutral pH value. The product was dried under reduced pressure at room temperature.

6. Synthesis of SBA–ALA and SBA–LYS

The synthesis followed the description of the amino acid coupling with 652.2 mg Fmoc-Ala-OH and 1237.4 mg Fmoc-Lys(Fmoc)-OH, resulting in SBA–NH–Ala-Fmoc and SBA–NH–Lys(Fmoc)-Fmoc. It was completed by the removal of the Fmoc protective group, yielding 385.9 mg of SBA-ALA and 295.7 mg of SBA–LYS.

7. Synthesis of SBA–GLU

For the amino acid coupling, 1021.4 mg Fmoc-Glu(2-PhiPr)-OH were utilized. The Fmoc group was cleaved first followed by the secession of the 2-PhiPr group, as described above. This led to a yield of 330.0 mg of SBA–GLU.

B. Characterization of the functionalized silica materials

For the characterization of the obtained functionalized silica materials, we employ the cross polarization (CP) and magic angle spinning (MAS) techniques to measure ^{13}C solid-state NMR spectra. In Fig. 2(a), we see that the ^{13}C CP MAS spectrum of SBA–APT exhibits resonances at 9, 21, and 42 ppm, which can be assigned to the carbons of the APTES linker. Furthermore, the weak signals at 18 and 59 ppm can be attributed to noncondensed ethoxy groups of APTES or tetraethyl orthosilicate (TEOS). These signals are preserved, albeit with altered intensities, in the spectra of the amino-acid functionalized materials, indicating that such groups are still attached to the surface after the coupling protocol. However, using the CP technique hampers quantitative statements. In Fig. 2(b), the ^{13}C CP MAS spectrum of SBA–ALA shows further signals at 27, 52, and 174 ppm, which can be attributed to the carbon atoms of Ala. In particular, the resonance at 174 ppm indicates the formation of an amide bond and, hence, the successful coupling of the amino acid to the silica surface. The remaining two signals are attributed to the carbon skeleton of Ala. The spectrum SBA–LYS is displayed in Fig. 2(c). In addition to the signals from the starting material, we detect resonances with chemical shifts of 27, 34, 44, 54, and 176 ppm. These signals can be attributed to Lys. The signal of the missing sixth carbon overlaps with that of the linker around 23 ppm.

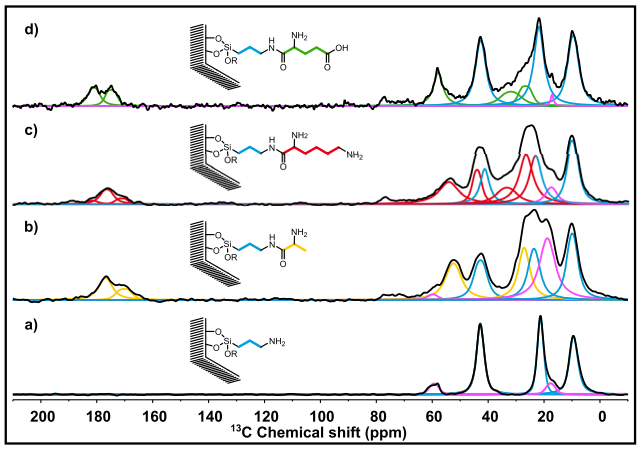

FIG. 2. ^{13}C CP MAS spectra (black lines) of the starting material and the prepared amino-acid functionalized silica materials: (a) SBA–APT, (b) SBA–ALA, (c) SBA–LYS, and (d) SBA–GLU. The blue signals result from the carbons of the APTES linker, and the yellow, red, and green resonances are attributed to Ala, Lys, and Glu, respectively. The pink signals are caused by residual ethoxy groups of noncondensed APTES or TEOS. The spinning rates are 6 kHz for SBA–APT and 10 kHz for the other samples.

The signals with the chemical shifts of 23, 27, 34, 44, and 54 ppm result from the carbon chain, whereas that at 176 ppm is characteristic for the carbon in the amide bond. Figure 2(d) presents the spectrum of SBA–GLU. While the signals at 27, 32, and 58 ppm can be assigned to the carbon chain between the amide bond and the carboxyl functionality, the latter groups cause the resonances at 175 and 181 ppm, respectively. The signal at 58 ppm overlaps with that of noncondensed ethoxy groups. Thus, the ^{13}C CP MAS spectra indicate successful binding of the amino acids to the surface of the SBA material.

To further analyze the synthesized materials, we use elemental and thermogravimetric analyses and nitrogen gas adsorption. Details of these characterizations can be found in the supplementary material. The results are compiled in Table I. The thermal analyses reveal that the starting material SBA–APT features 2.1 mmol/g APTES linkers and that 22% (SBA–ALA), 19% (SBA–LYS), and 17% (SBA–GLU) of the linkers are occupied by amino acids in the functionalized materials. Nitrogen gas adsorption yielded information about the pore geometries. As expected, the pore volume and the pore diameter are reduced by the coupling of the amino acids. However, all studied host materials still have similar pore diameters of ~6 nm. Because the Barrett–Joyner–Halenda (BJH)[83] and nonlocal density functional theory (NLDFT)[84] methods yield somewhat different pore diameters (see the supplementary material), we follow previous works[62,63] and give the average values in Table I. Furthermore, we find that the amino-acid functionalization leads to a decrease in the specific surface area. Combining all the information, it is possible to calculate the surface density of the functional groups. For SBA–APT, we obtain an APTES linker density of 2.3 nm^{-2}. For the amino-acid functionalized materials, the achieved linker occupancies of ~20% correspond to Ala, Lys, or Gly surface densities in the range 0.4–0.5 nm^{-2}.

III. NMR BACKGROUND

In ^{2}H NMR studies, the quadrupolar frequencies of the deuterons are given by[85]

$$\omega_Q(\theta,\phi) = \pm\frac{\delta}{2}\left[3\cos^2\theta - 1 - \eta\sin^2\theta\cos(2\phi)\right]. \quad (1)$$

Here, the ± signs correspond to two allowed transitions between the Zeeman levels of these $I = 1$ nuclei. Furthermore, δ and η denote the anisotropy and asymmetry parameters of the quadrupolar interaction tensor of the deuterons, while the angles θ and ϕ characterize the orientation of this tensor in relation to the applied magnetic field B_0. In the studied samples, chemical exchange distributes the deuterons among the O–D bonds of the water molecules and the N–D bonds of the surface groups, for which the quadrupolar interaction tensors are nearly axially symmetric, i.e., $\eta \approx 0$. Thus, the quadrupolar frequencies can be written as

$$\omega_Q(\theta_n) \approx \pm\frac{\delta_n}{2}\left(3\cos^2\theta_n - 1\right), \quad (2)$$

where the index n distinguishes the different deuteron species.

TABLE I. Results from elemental and thermogravimetric analyses and from nitrogen gas adsorption of the functionalized silica materials (see the supplementary material for details). The loading with the functional groups and the fraction of the occupied linkers from the thermal analyses and the pore geometries from the gas adsorption are given. The surface area and pore volume were obtained from the BJH and Gurvich methods, respectively. The pore diameters are specified as the average values from the BJH and the NLDFT methods.[62,63] The surface density gives the number of functional surface groups per nm^2.

Sample	Loading by N content in mmol g^{-1}	Occupied linkers in %	Specific surface area in m^{2}g^{-1}	Pore volume in cm^{3}g^{-1}	Pore diameter in nm	Surface density in nm^{-2}
SBA–APT	2.10[a]	⋯	545	0.74	6.8	2.3[a]
SBA–ALA	0.46[b]	22	410	0.57	5.9	0.5[b]
SBA–LYS	0.40[b]	19	389	0.55	5.8	0.4[b]
SBA–GLU	0.35[b]	17	339	0.52	5.6	0.4[b]

[a]Linker.
[b]Amino acid.

A. ^{2}H spin–lattice relaxometry

In the ^{2}H SLR experiments, we probe the recovery of the ^{2}H magnetization after saturation. Because the magnetization buildup may involve dynamically distinguishable deuteron species n, we fit the observed buildup $M(t_d)$ to a sum of stretched exponential functions,

$$M(t_d) = M_\infty - \sum_n m_n \exp\left[-\left(\frac{t_d}{T_{1,n}}\right)^{\beta_{1,n}}\right]. \quad (3)$$

Here, M_∞ is the equilibrium magnetization and the contributions from the deuteron species are characterized by their magnetization shares m_n, relaxation times $T_{1,n}$, and stretching parameters $\beta_{1,n}$. To account for the possibly nonexponential ^{2}H SLR of the deuteron species ($\beta_{1,n} < 1$), we utilize the Γ function to calculate the mean ^{2}H SLR times $\langle T_{1,n}\rangle = (T_{1,n}/\beta_{1,n})\Gamma(1/\beta_{1,n})$ from the fit parameters.

^{2}H SLR analysis provides access to the spectral densities of rotational motions. Specifically, for exponential buildup steps, the ^{2}H SLR time T_1 at a Larmor frequency ω_L amounts to

$$\frac{1}{T_1(\omega_L)} = \frac{2}{15}\delta^2\left[J_2(\omega_L) + 4J_2(2\omega_L)\right], \quad (4)$$

where the spectral density $J_2(\omega)$ is related to the correlation function of the second-order Legendre polynomial, $F_2(t)$, by Fourier transformation.[86,87] In temperature-dependent measurements, a $T_1(T)$ minimum is found when the corresponding correlation time obeys $\tau \approx 0.6/\omega_L$, largely independent of the shape of the spectral density. Hence, dynamics in the nanoseconds regime is observed for typical field strengths B_0 and, thus, Larmor frequencies ω_L.

The determination of temperature-dependent correlation times from $T_1(T)$ data relies on the information about the functional form of $J_2(\omega)$. For the water reorientation in mesoporous silica, dynamical heterogeneities lead to nonexponential correlation functions. Motivated by BDS findings,[20,36,61] we describe the corresponding non-Lorentzian spectral densities based on the Cole–Cole (CC) function,

$$J_2^{cc}(\omega) = \frac{\omega^{-1}\sin\left(\frac{\pi}{2}\beta_{cc}\right)(\omega\tau_{cc})^{\beta_{cc}}}{1 + 2\cos\left(\frac{\pi}{2}\beta_{cc}\right)(\omega\tau_{cc})^{\beta_{cc}} + (\omega\tau_{cc})^{2\beta_{cc}}}. \quad (5)$$

Here, τ_{cc} and β_{cc} are the time constant and the width parameter, respectively. The former can be identified with the peak position τ_p of the underlying symmetric CC distribution of correlation times $G_{cc}(\log\tau)$, and the latter can be determined from the height of the $T_1(T)$ minimum.[88]

B. ^{2}H line shape analysis and solid-echo intensities

^{2}H NMR spectra depend on the rate and geometry of molecular reorientation so that ^{2}H LSA yields valuable insight into both aspects.[89] For isotropic reorientation related to the structural relaxation of liquids, broad Pake spectra and narrow Lorentzian lines are observed for correlation times $\tau \gg 1/\delta$ and $\tau \ll 1/\delta$, respectively. On the other hand, uniaxial rotation of side groups causes only partial averaging of the quadrupolar interaction, leading to a crossover between broad and narrow Pake spectra when τ crosses the experimental time scale $1/\delta \approx 1\ \mu$s upon heating. Thus, we expect different high-temperature line shapes for water and framework deuterons, which will be used for a discrimination of the respective signal contributions.

Such ^{2}H NMR line shape transitions are accompanied by a reduced solid-echo intensity (SEI).[89,90] This effect is based on the fact that ω_Q fluctuations owing to molecular reorientation during the dephasing and rephasing periods of the applied solid-echo pulse sequence interfere with successful echo formation. Thus, an attenuation of ^{2}H solid-echo signals is indicative of rotational motion in the microseconds regime.[89,90]

C. Details of the ^{2}H NMR experiments

The ^{2}H NMR measurements were performed on two home-built spectrometers working at similar ^{2}H Larmor frequencies of $2\pi \cdot 46.1$ and $2\pi \cdot 46.7$ MHz, respectively. The length of the 90° pulses amounted to ~2.5 μs in all experiments. The ^{2}H NMR spectra were recorded with the solid-echo sequence $90^\circ_x - \Delta_e - 90^\circ_y$, utilizing an echo delay of $\Delta_e = 20\ \mu$s. For the ^{2}H SLR studies, we employed the saturation-recovery sequence in combination with solid-echo detection. All measurements were performed from low to high temperatures. The temperature was controlled by flow cryostats for gaseous nitrogen and stabilized to ±0.1 K with an absolute accuracy of ±1 K. Further details of the ^{2}H NMR setups can be found in previous works.[72,75]

For the preparation of the NMR samples, the functionalized mesoporous silica was first carefully dried in vacuum.[91] Afterward, we added D_2O (Sigma-Aldrich) in appropriate amounts to achieve filling levels between 80% and 100% of the pore volumes, as calculated based on the mass of the dry silica materials and the specific pore volumes (see Table I). Directly after the addition of water, the filled mesoporous silica was sealed in NMR tubes. To ensure an equilibrium distribution of the water in the samples, we observed shelf times of several days prior to the measurements.

While the SBA–ALA and SBA–LYS samples had no freezable water outside the silica particles, the ^{2}H NMR signals revealed that minor amounts of excess water caused some external ice when cooling the SBA–GLU and SBA–APT samples. However, previous studies on water in silica pores showed that the existence of ice outside the pores does not interfere with the analysis of the dynamics of water inside the pores because the exchange between both water species is negligible and the signal of the external and internal water fractions can be readily discriminated based on largely different T_1 times.[62,72] Therefore, we do not address aspects related to minor amounts of external ice in the following.

IV. RESULTS

Prior to presenting our ^{2}H NMR results, it is useful to provide further information about the deuteron distributions in the studied samples. As aforementioned, chemical exchange leads to an ongoing redistribution of the deuterons between the water molecules and the framework groups. The equilibrium fractions of the different deuteron species can be calculated based on the water content of the studied samples and the surface density of the functional groups (see

Table I). Assuming that there are no extreme acidic or basic conditions inside the pores, we estimate that roughly 90% of the deuterons belong to the O–D bonds of the water molecules and the remainder to the N–D bonds of the surface groups. Expecting that the amide, amino, and carboxyl groups are ionized and depending on the type of the functionalization, we expect about 1% amide deuterons in the peptide bonds between the linker units and the amino acids and ~8%–13% of the deuterons in the largely protonated amine groups (ND_3^+) of the residues.

A. ^{2}H NMR solid-echo spectra

To investigate the dynamical behaviors of the different deuteron species, we first perform ^{2}H LSA. Exemplarily, Fig. 3 shows the ^{2}H solid-echo spectra of D_2O in SBA–ALA at various temperatures. Based on the Gibbs–Thomson relation, we anticipate that partial crystallization occurs near 260 K and results in coexisting liquid and crystalline water phases inside the pores before the liquid turns into a glass at low temperatures. Moreover, we expect that the amide deuterons of the peptide bonds are hardly mobile, while the deuterons in the (protonated) amine groups are subject to uniaxial rotations of these groups around the associated C–N bonds.[92,93] Accordingly, the ^{2}H NMR spectra of D_2O in SBA–ALA comprise several line shape patterns, depending on the temperature.

At 130–150 K, we observe superpositions of broad and narrow Pake spectra. The broad Pake component reveals deuterons in static chemical environments. It can be described by an anisotropy parameter of $\delta = 2\pi \cdot 161$ kHz and an asymmetry parameter of $\eta = 0.10$, typical of the O–D bonds in water.[18] Thus, the broad Pake spectrum results from the glassy—or at least highly viscous—and crystalline fractions of confined water at low temperatures. In addition, it may receive contributions from static N–D bonds of the framework, which remain, however, unresolved because the amide deuterons constitute only 1% of the deuterons and exhibit similar anisotropy and asymmetry parameters of $\delta = 2\pi \cdot 147$ kHz and $\eta = 0.17$.[52] The narrow Pake spectrum exhibits an anisotropy parameter of $\delta \approx 2\pi \cdot 40$ kHz and indicates fast uniaxial reorientation. Therefore, we assign it to the ND_2/ND_3^+ groups, which show rapid rotation around the associated C–N bonds.[52,65]

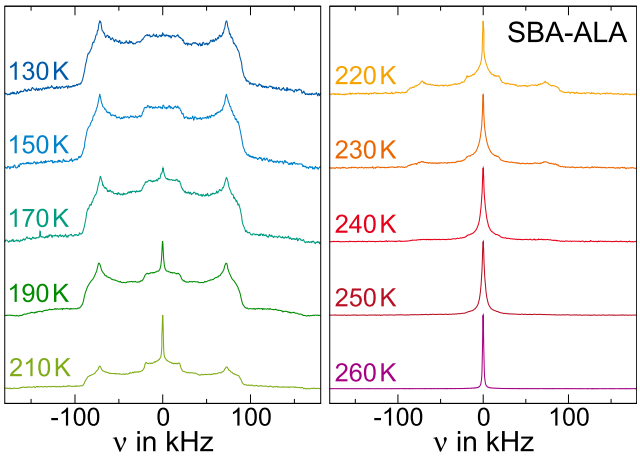

FIG. 3. ^{2}H NMR solid-echo spectra of D_2O in SBA–ALA at temperatures between 130 and 260 K. All spectra are scaled to show the same maximum spectral intensity.

When the temperature is increased, the broad Pake spectrum of the water deuterons is gradually replaced by a Lorentzian line, indicating that the correlation times of molecular reorientation in both confined water phases cross the time scale of the experiment, $\tau = 1/\delta \approx 1$ μs. In harmony with the findings in Fig. 3, previous ^{2}H NMR studies revealed that the glassy slowdown of liquid water in silica pores is characterized by correlation times of $\tau \approx 1$ μs near 200 K.[62,72,94] However, the water molecules of the confined crystal also show substantial reorientation dynamics. Specifically, they would contribute a broad Pake spectrum up to the melting point near 260 K if they were static on the experimental time scale. Instead, we observe that the broad Pake gradually loses intensity upon heating until it vanishes near 240 K, indicating that the confined crystal does not show reorientation dynamics slower than microseconds at this temperature either.

The inspection of Fig. 3 further suggests that the narrow Pake spectrum also disappears when the temperature is increased through 240 K. In the supplementary material, a closer analysis reveals that this is true for the other studied modifications, whereas the first impression is misleading for SBA–ALA, which shows a narrow Pake component even at room temperature. A further narrowing of this line shape component results when, superimposed on the fast uniaxial rotation, the rotation axes themselves, i.e., the C–N bonds, become mobile on the microseconds time scale. These observations are consistent with the expectation that Glu and Lys with larger residues show higher mobility than Ala with a methyl group residue. Alternatively, the narrow Pake pattern disappears when the time scale of the deuteron exchange between the residues and water reaches that of the line shape experiment upon heating. However, we do not expect strongly diverse deuteron exchange rates for the studied amino acids, which would explain the observed difference. Conversely, at $T < 240$ K, clearly distinguishable residue and water signals show that the deuteron exchange is slow, which will allow us to disentangle these contributions in the ^{2}H SLR analysis in Sec. IV B. Finally, we see in Fig. 3 that the narrow Pake spectrum has a reduced intensity at 130 K, suggesting that the uniaxial rotation starts to freeze on the microseconds time scale.

In Fig. 4, we display the ^{2}H NMR spectra of D_2O in all studied pores at 180 and 220 K. At the lower temperature, the spectra comprise a broad Pake spectrum from the viscous and crystalline D_2O fractions and a narrow Pake spectrum from the ND_2/ND_3^+ groups, largely independent of the type of the modification. An integration of the respective spectral intensities shows that the narrow Pake spectrum contributes about 3%–5% to the total intensity. This contribution is a little less than expected based on the above estimates for the proportions of the different deuteron species. Unlike in the other confinements, a small and narrow Lorentzian line exists in SBA–ALA down to 170 K (see also Fig. 3). It indicates a minor deuteron fraction with high mobility, but we cannot make an unambiguous assignment at present. A comparison of the spectra at 220 K suggests that the observed line shape transition associated with the confined water dynamics occurs at the highest

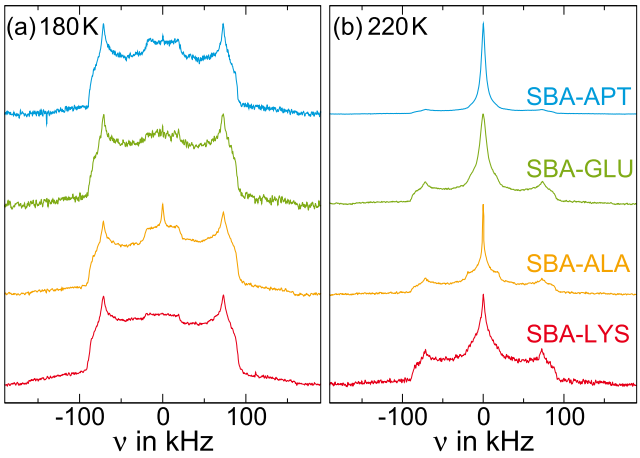

FIG. 4. ^{2}H NMR solid-echo spectra of D_2O in modified silica pores at (a) 180 K and (b) 220 K. Results for SBA–APT, SBA–GLU, SBA–ALA, and SBA–LYS are compared. All spectra are scaled to show the same maximum spectral intensity.

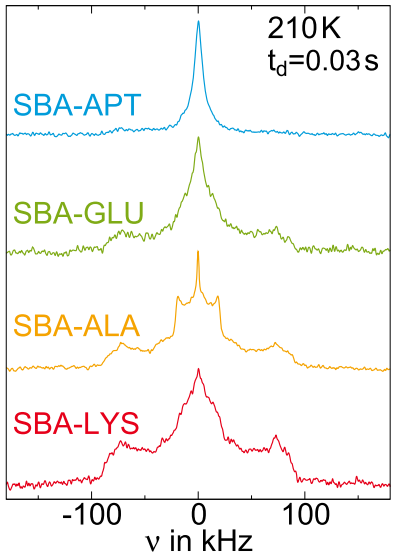

FIG. 5. Partially relaxed ^{2}H NMR solid-echo spectra of D_2O in modified silica pores at 210 K. Results for SBA–APT, SBA–GLU, SBA–ALA, and SBA–LYS are compared. All spectra are measured with a relaxation delay of $T_{1,l} < t_d = 0.03\ \text{s} < T_{1,c}$ between the saturation of the magnetization and the acquisition of the signal and scaled to show the same maximum spectral intensity.

temperature in SBA–LYS and at the lowest temperature in SBA–APT, while Ala and Glu functionalizations lead to intermediate behaviors.

Because the line shape contributions of the liquid and crystalline water fractions overlap in the conventional ^{2}H NMR spectra recorded after full relaxation of the magnetization, we exploit that the buildup of the magnetization occurs much faster for the liquid water than for the crystalline water (see Sec. IV B) to disentangle their signals in saturation-recovery experiments under partial relaxation conditions. Specifically, we use a delay t_d between the destruction of the magnetization and the acquisition of the signal for which the contributions of the liquid and crystalline fractions have recovered to major and minor extents, respectively. Therefore, we expect that such partially relaxed ^{2}H NMR spectra unveil the line shape of the liquid water, supplemented by possible contributions from the deuterons of the surface groups, while ice signals are suppressed. In Fig. 5, we compare the partially relaxed spectra of D_2O in various confinements measured at 210 K for a recovery delay t_d of 30 ms. The liquid water fraction gives rise to a broad Pake spectrum in SBA–LYS and to a narrow Lorentzian line in the SBA–APT, indicating correlation times of $\tau \gg 1\ \mu$s and $\tau \ll 1\ \mu$s, respectively, while the line shapes for the Ala and Glu confinements are intermediate between these limiting cases. These findings show that the time scale of water reorientation in the liquid phase noticeably depends on the type of the functionalization.

B. ^{2}H spin–lattice relaxation

To gain further insight into the reorientation dynamics of the various deuteron species, we perform ^{2}H SLR experiments. Figure 6 shows the buildup of the magnetization for D_2O in SBA–GLU at exemplary temperatures. Evaluating the total signal intensity, we find that the magnetization buildup is single exponential at 270 K. By contrast, it occurs in two steps at 185 K, indicating the coexistence of liquid ($T_{1,l}$) and crystalline ($T_{1,c}$) water phases inside the pores at lower temperatures. Further relaxation steps from the deuterons of the surface groups are not resolved in the analysis of the total signal intensity, even though we observed their signal contributions in the spectra.

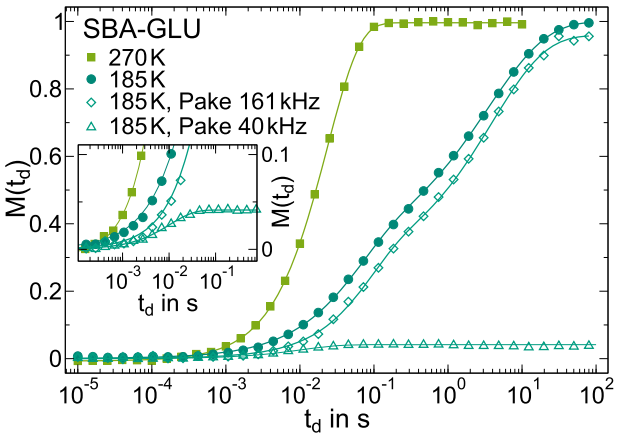

FIG. 6. Buildup of normalized ^{2}H magnetization $M(t_d)$ for D_2O in SBA–GLU at 185 and 270 K. In addition to the buildup of the total signal intensity (solid symbols), results from a spectrally resolved analysis are shown for the lower temperature (open symbols). In detail, the buildup curves associated with the horns of the narrow and broad Pake spectra with $\delta = 2\pi \cdot 40$ and $\delta = 2\pi \cdot 161$ kHz, respectively, are displayed. To illustrate the different spectral intensities of these line shape components, both curves are scaled to their respective contribution to the whole spectrum. The inset shows a zoomed-in view, which focuses on the buildup of the narrow Pake intensity. The solid lines are fits to Eq. (3).

Therefore, we perform a spectrally resolved SLR analysis at lower temperatures where the line shape contributions of the different deuteron species can be clearly distinguished. Specifically, we determine the buildup curves associated with the horn intensities of the narrow and broad Pake spectra with $\delta = 2\pi \cdot 40$ kHz and $\delta = 2\pi \cdot 161$ kHz, respectively. This spectrally resolved analysis reveals a third buildup step associated with the narrow spectrum of the Glu deuterons, which has a small amplitude and occurs at short times (see the inset of Fig. 6), whereas the results for the broad spectrum from the water deuterons highly resembles those from the total signal intensity, confirming that the bimodal nature reflects the coexisting liquid and frozen water fractions.

For a quantitative analysis, we fit the low-temperature buildup curves $M(t_d)$ to Eq. (3). We find that the fit results for the buildup of the broad Pake intensity agree with those for the total spectral intensity within the error margins. Therefore, it is sufficient to extract the $T_{1,l}$ and $T_{1,c}$ values from the total intensity in the following analysis. The SLR times associated with the narrow Pake spectrum are very similar for all functional groups and much shorter than $T_{1,l}$ and $T_{1,c}$ at sufficiently low temperatures. Exemplary data from the different analyses and samples are provided in the supplementary material. The observation that the various deuteron species have different $T_{1,n}$ times implies that the chemical exchange between them is slow on the time scale of the magnetization buildup at these temperatures, which means that a SLR analysis informs about the respective dynamics. This will be discussed in more detail at the end of this section. In passing, we note that the magnetization associated with the narrow Pake pattern builds up in a stretched exponential manner, indicating that a distribution of correlation times $G(\log \tau)$ governs the uniaxial rotation of the side groups.

In Fig. 7, we show the mean ^{2}H SLR times for the water deuterons in the modified silica pores together with those for a native SBA-15 pore with a similar diameter of 5.4 nm.[62] We note that the properties of the native SBA-15 material were determined in previous work,[63] revealing a pore diameter of 5.4 nm, which differs from the value of 6.0 nm provided by the supplier and given in earlier work.[62] Except for SBA–ALA, we observe exponential SLR characterized by a single T_1 time above 260 K, while the $\langle T_{1,l} \rangle$ and $\langle T_{1,c} \rangle$ times of the liquid and crystalline water fractions, respectively, can be clearly distinguished at sufficiently low temperatures. First, we focus on the results for $\langle T_{1,l} \rangle$. For all samples, we observe $\langle T_{1,l} \rangle$ minima in the range 225–250 K, indicating correlation times of $\tau_p = 0.6/\omega_L \approx 2$ ns. The SLR results for SBA–APT are in reasonable agreement with those for the native pore over the whole temperature range. A minor difference is that the $\langle T_{1,l} \rangle$ minimum occurs at a slightly lower temperature for SBA–APT, indicating a mild speedup of water reorientation relative to native SBA-15. By contrast, the $\langle T_{1,l} \rangle$ minima are shifted to higher temperatures in the amino-acid functionalized pores (see Table II), and hence, water reorientation slows down. Altogether, we observe the largest shift and strongest slowdown for the Lys followed by the Ala and Glu functionalizations, while there is a minor speedup for SBA–APT. These SLR findings are consistent with the above LSA results.

Moving on to the results for the crystalline water fraction inside the pores, we see that the $\langle T_{1,c} \rangle$ times are essentially independent of the type of functionalization. They agree with those reported for the

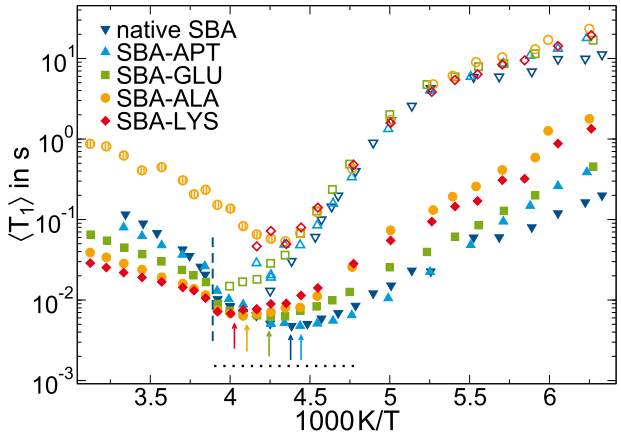

FIG. 7. Temperature-dependent mean ^{2}H SLR times $\langle T_1 \rangle$ for D_2O in silica pores with the indicated modifications. Solid symbols mark the $\langle T_{1,l} \rangle$ times of the liquid D_2O fractions, while open symbols depict the $\langle T_{1,c} \rangle$ times of the crystalline D_2O fractions in the pores. The striped symbols are used to indicate a different SLR component for the Ala confinement at the higher temperatures of the studied range. For comparison, the ^{2}H SLR times of D_2O in a native silica pore with a diameter of 5.4 nm are included.[62] The arrows mark the positions of the $\langle T_{1,l} \rangle$ minima, which are given in Table II. The horizontal black dotted line illustrates the height of the T_1 minimum for $\omega_L = 2\pi \cdot 46.1$ MHz and $\delta = 2\pi \cdot 161$ kHz in the case of a Lorentzian spectral density $J_2(\omega)$. The vertical blue dashed line marks the melting point $T_m = 258$ K of the internal ice in the native confinement.[62]

internal ice in the native pore, whereas they are much shorter than those reported for external ice, which amount to about 1000 s at 200 K,[62] and also much shorter than those of hexagonal and cubic ices in the bulk.[95,96] These discrepancies mean that the internal ice can be clearly distinguished from external and bulk ice phases in the ^{2}H SLR analyses. Moreover, it implies that water reorientation is faster for the confined ice than for hexagonal or cubic bulk ices, possibly as a consequence of a perturbed ice structure under nanoscale geometrical restriction. Relating to the temperature dependence of $\langle T_{1,c} \rangle$, we find that a steeper slope is replaced by a flatter one upon cooling through ~200 K. On first glance, this suggests a change in some property of the internal ice. However, a reason for such a change is not obvious. An alternative interpretation is based on

TABLE II. Temperatures T_{min} of the $\langle T_{1,l} \rangle$ minima, width parameters β_{cc} of the CC spectral densities, and Arrhenius fit parameters τ_0 and E_a from the interpolations of the ^{2}H NMR correlation times in Fig. 9 for the liquid D_2O fraction in silica pores with the indicated modifications. The data for D_2O in the native SBA-15 pores were obtained in previous work.[62]

	T_{min} in K	β_{cc}	τ_0 in 10^{-30} s	E_a in eV
Native SBA	228	0.37	9.8	0.92
SBA–APT	225	0.38	81	0.86
SBA–GLU	236	0.30	0.024	1.07
SBA–ALA	244	0.28	1.6	1.02
SBA–LYS	248	0.25	40	0.98

the fact that the ^{2}H NMR line shape transition occurs near 200 K. Thus, an exchange of magnetization between the liquid and crystalline water fractions inside the pores can occur below this temperature as a consequence of spin diffusion mediated by non-averaged dipolar interactions between the nuclear spins. If the latter situation applies, the $\langle T_{1,l}\rangle$ and $\langle T_{1,c}\rangle$ times do no longer inform about the true SLR behaviors and, thus, about the water dynamics of the respective phases below 200 K.

In Fig. 7, we also see that the onset of bimodal SLR occurs near T_m = 258 K, the melting point of ice inside the native pores,[62] in accordance with our ascription to partial crystallization. Two further observations related to this phenomenon are notable. First, $\langle T_{1,l}\rangle$ of the liquid fraction shows a mild jump at this temperature. While the water molecules explore the whole pore volume above T_m, the liquid water is sandwiched between the pore walls and the ice core below. Hence, one may expect that this reduction of the accessible pore volume to a narrow interfacial layer results in some decline in the average water mobility and, on the high-temperature flank of the minimum, in a decrease in $\langle T_{1,l}\rangle$, rationalizing the observed weak drop. Second, except for SBA–GLU, the $\langle T_{1,c}\rangle$ step of the crystalline fractions does not set in exactly at T_m but at a somewhat lower temperature.

Before we discuss the reason for the latter effect, we come back to the additional slow SLR step in SBA–ALA, which occurs at ambient temperatures and indicates an exceptionally fast deuteron species. In the supplementary material, a buildup curve shows that the slow step amounts to about 5% of the signal. Moreover, a spectral analysis reveals that the additional contribution has a Lorentzian shape. Thus, it stands to reason that the slow SLR step at high temperatures and the narrow Lorentzian line observed down to 170 K (see Fig. 3) have the same origin. While this does not clarify the nature of the fast deuteron species, effects on the analysis of the water dynamics are minor because of the small contribution to the total signal.

Finally, we ascertain the contributions of the liquid and crystalline water fractions to the signal intensity in the SLR measurements, whereby the minor contributions from the framework deuterons are neglected. Because the signals are obtained from the solid-echo pulse sequence, they depend not only on the amount but also on the dynamics of the deuteron species. Specifically, the nominal signal contribution of a deuteron species is attenuated when it is involved in rotational motion, which occurs during the echo experiment, i.e., in the microseconds regime (see Sec. III B).

Figure 8 shows the solid-echo signal contributions from the liquid and crystalline D_2O fractions for all but the Ala functionalization. Here, we leave out the results for SBA–ALA because the additional SLR contribution of this sample spoils the analysis of the step heights. We see a discontinuity of the temperature dependence near T_m, which marks the segmentation into liquid and crystalline water species during partial crystallization. When cooling at $T < T_m$, the solid-echo intensity of the liquid fraction first rapidly decreases before it mildly recovers, resulting in a broad minimum near 200 K, which is indicative of microsecond dynamics. Closer inspection reveals that the minimum occurs at a somewhat higher temperature for SBA–LYS than for SBA–GLU and SBA–APT. This implies that water dynamics is slower in the former than in the latter confinements and confirms the above findings for the narrowing of the NMR spectra and the temperatures of the $T_{1,l}$ minima.

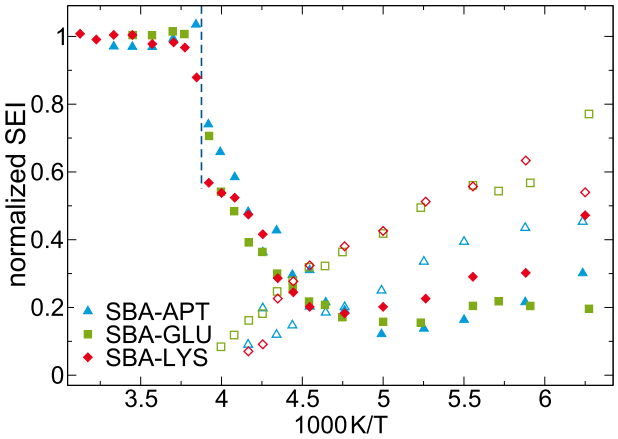

FIG. 8. Temperature dependence of the solid-echo intensity (SEI) contributions for D_2O in SBA–APT, SBA–GLU, and SBA–LYS. All values are normalized to their respective high temperature plateau and corrected for the Curie factor. The contributions from the liquid (solid symbols) and crystalline (open symbols) water fractions were disentangled by fitting the buildup of the total signal intensity with two-step relaxation [see Eq. (3)]. The dashed line marks the melting point T_m = 258 K of D_2O in the native SBA-15 sample.[62]

The solid-echo intensity of the crystalline fraction is very small near T_m and continuously increases upon cooling. On first glance, this observation implies that the crystalline fraction grows when the temperature is decreased. However, such growth is not detected by other experimental methods. Alternatively, the findings can be rationalized when we assume that the rotational motion occurs on the microseconds scale near T_m and decelerates upon cooling so that it interferes less and less with the solid-echo formation. The latter scenario should also manifest itself in line shape changes. Consistently, we show in the supplementary material that the broad Pake spectrum of the crystalline water fraction exhibits very sharp Pake horns up to about 220 K, which, however, become rounded and flattened at 240–250 K, suggesting that the reorientation dynamics enters the time window. Furthermore, this argument is consistent with the time scales of water reorientation in distorted ice phases observed in BDS studies.[37,94] Whatever the reason of the low signal of the crystalline fraction near T_m, it impedes its disclosure in the buildup curves, providing a rationale for the above observation that this contribution is resolved only somewhat below T_m in most of the studied samples (see Fig. 7).

C. Determination of correlation times

Equation (4) enables a determination of rotational correlation times for single exponential steps in magnetization buildup curves. In the supplementary material, we show that $\beta_{1,l} \approx 1$ indicates a single exponential buildup and, hence, $T_{1,l} \equiv \langle T_{1,l}\rangle$ for the liquid fraction down to ~200 K, whereas $\beta_{1,c} < 1$ is found for the crystalline fraction in the whole temperature range. Therefore, we restrict a quantitative SLR analysis to liquid water at temperatures near the $T_{1,l}$ minimum, where single exponential behavior is obeyed. Reinspecting Fig. 7, we see that the minimum values of $T_{1,l} \equiv \langle T_{1,l}\rangle$

do not conform to a Lorentzian shape of the spectral density $J_2(\omega)$. Therefore, we use the CC spectral density to account for the dynamical heterogeneity and determine the CC width parameter β_{cc} from the height of the $T_{1,l}$ minimum. In Table II, we see that the β_{cc} values are small between 0.25 for SBA–LYS and 0.38 for SBA–APT, indicating that the reorientation dynamics of the confined waters are strongly heterogeneous.

Using the thus obtained spectral densities $J_2^{cc}(\omega)$ in Eq. (4), we determine the peak correlation times $\tau_p = \tau_{cc}$ from the $T_{1,l}$ data. However, it is necessary to consider possible changes in the shape of the spectral density at T_m so that the accessible dynamic range is limited not only by nonexponential behavior at low temperatures but also by partial crystallization at high temperatures. In Fig. 9, the available peak correlation times τ_p are compared with those from an analogous approach to the liquid water fraction in native SBA-15 pores. We see that the APTES modification results in a mild speedup of water reorientation relative to the native pore, while the amino-acid functionalizations lead to rotation dynamics that are up to two orders of magnitude slower. Explicitly, the slowdown is most pronounced for basic Lys, followed by neutral Ala and acidic Glu. These findings are in accordance with the above observations for the narrowing of the NMR spectra and the temperatures of the $T_{1,l}$ minima.

In the relatively narrow dynamic range of the present SLR analysis, the temperature dependence can be approximated by an Arrhenius law,

$$\tau_p(T) = \tau_0 \exp\left(\frac{E_a}{k_B T}\right). \tag{6}$$

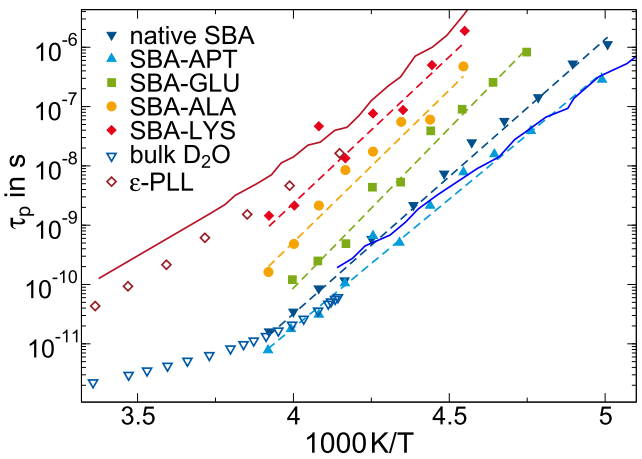

FIG. 9. Peak correlation times τ_p for the reorientation dynamics of liquid D_2O fractions in silica pores with the indicated modifications, as obtained from ^2H SLR analysis. Furthermore, data from analogous approaches to D_2O in native SBA-15 pores with a diameter of 5.4 nm[62] and in a mixture with ε-L-polylysine are included.[52] The dashed lines are Arrhenius fits. For comparison, ^2H NMR results for bulk D_2O are shown.[97] Moreover, the solid lines depict rotational correlation times from BDS studies on (blue) H_2O in native MCM-41 silica pores with a diameter of 2.1 nm[21] and (red) a 40 wt. % aqueous solution of the amino acid L-lysine, more precisely, of a BDS process attributed to the structural relaxation of H_2O in this mixture.[98]

However, the resulting fit parameters imply deviations from an Arrhenius behavior in a broader temperature range (see Table II). Specifically, the fits yield E_a values of ~1 eV, which are much higher than the characteristic activation energies for hydrogen-bond breaking, and the pre-exponential factors τ_0 are much smaller than the inverse attempt frequencies of thermally activated processes. Such unusual values are known to result for molecular glass-forming liquids showing super-Arrhenius temperature dependence.

To further assess the outcome of the SLR analysis, we include literature data for water reorientation in Fig. 9. The rotational motions of the liquid D_2O fractions in native SBA-15 and SBA-APT resemble those from a BDS study on unfreezable H_2O in very narrow silica pores with a diameter of 2.1 nm.[21] Furthermore, they are in agreement with ^2H NMR rotational correlation times for D_2O as a bulk liquid.[97] On the other hand, the correlation times of D_2O reorientation in SBA–LYS are similar to those of a BDS process, which was reported for an aqueous solution of the amino acid L-lysine and attributed to the structural relaxation of water in the mixture.[98] In both cases, LYS forms some kind of soft confinement for the water motion: The amino acid is linked to the silica walls in the present approach and its structural relaxation is much slower than that of water in the BDS study.[98] Accordingly, our findings for SBA–LYS also resemble those obtained from an analogous ^2H SLR approach to D_2O in a dynamically asymmetric mixture with ε-L-polylysine,[52] although it was argued that the latter are affected by water and peptide dynamics because of the fast deuteron exchange between both constituents.

Therefore, we need to scrutinize to what extent chemical exchange distorts the present SLR analysis. In the limit of fast exchange between various species n with magnetization shares m_n and SLR times $T_{1,n}$, one finds single exponential SLR characterized by the common rate,

$$\frac{1}{T_1} = \frac{1}{M_\infty} \sum_n \frac{m_n}{T_{1,n}}. \tag{7}$$

Hence, the observed T_1 value of a species will be affected significantly if it is in rapid exchange with another species, which has a higher abundance and a significantly different SLR rate. In our samples, the deuterons of the liquid water exchange particularly with that of the surface groups. Accordingly, these deuteron species do not show distinguishable T_1 times above ~250 K. However, unlike in a previous study on an aqueous ε-L-polylysine solution,[52] the deuterons of the liquid outnumber those of the matrix and the SLR rates of these species hardly differ near the T_1 minimum. Therefore, we expect that the deuteron exchange weakly affects the $T_{1,l}$ values near the minimum. In particular, the temperatures of the $T_{1,l}$ minima should still reflect the time scale of water dynamics. On the other hand, the height of the $T_{1,l}$ minima may be altered by admixed contributions from the matrix deuterons. This will affect the CC width parameters β_{cc} extracted therefrom and, thus, lead to a somewhat erroneous temperature dependence of the correlation times τ_{cc}. Moreover, the fact that, in general, the observed T_1 values differ from the true values of the species near the onset of the bimodality,[99] i.e., when the limit of slow exchange does not yet fully apply, adds to the inaccuracy at temperatures not too far

below 250 K. Altogether, we conclude that our findings for the dependence on the water mobility on the surface chemistry are robust, while the obtained variation with temperature should be interpreted with caution. Yet, we showed that our results are in reasonable agreement with correlation times from dielectric measurements on similar systems,[21,52] indicating that the deficiencies are still tolerable.

V. CONCLUSION

We exploited the possibility to functionalize silica surfaces with amino acids to design biomimetic environments for water. Specifically, we synthesized porous confinements, which feature acidic Glu, neutral Ala, or basic Lys functional groups and have similar diameters of 5.6–5.9 nm. For the characterization of these host materials, we combined ^{13}C CP MAS NMR, elemental and thermogravimetric analyses, and nitrogen gas adsorption measurements. We found that the surface density of the APTES linkers amounted to 2.3 nm^{-2} in the starting material and that ~20% of the linkers were occupied by amino acids in the functionalized samples.

Our main goal was to characterize the water dynamics in these confinements in dependence on the functionalization and temperature. For this purpose, we performed ^{2}H LSA and SLR studies. While these approaches provided straightforward access to the rates and mechanisms of D_2O reorientation in native silica pores,[18,62,72] the analyses were more involved for the present functionalized confinements, which feature multiple deuteron species. Explicitly, partial crystallization resulted in a coexistence of liquid and crystalline D_2O fractions inside the pores and chemical exchange spread the deuterons not only over these water species but also over the amide and amine groups on the inner surfaces. Therefore, it was necessary to disentangle the ^{2}H NMR signals of the various deuteron species based on their diverse spin relaxations and spectral line shapes. In particular, we used the facts that the liquid and crystalline water fractions have very different T_1 times and that many of the N–D bonds are involved in fast uniaxial reorientation and, hence, produce Pake spectra with a reduced spectral width, which can be discriminated from the broad Pake spectra and the narrow Lorentzian lines from the O–D bonds of water. Moreover, we critically discussed to what extent chemical exchange between the deuteron species interferes with the possibility to separately study their dynamical behaviors.

Despite these difficulties, our ^{2}H LSA and SLR approaches yielded valuable insight into the reorientation dynamics of the liquid and crystalline water fractions coexisting inside the amino-acid functionalized confinements at reduced temperatures. The transitions of the line shape and the minima of the spin–lattice relaxation time and of the solid-echo signal intensity provided a consistent picture for the dependence of water dynamics on the surface chemistry. Specifically, the reorientation of the liquid water fraction is slowest near the Lys surface followed by the Ala and Glu confinements and, finally, the native pores. In total, this variation of the water mobility extends over about two orders of magnitude, essentially independent of temperature. Thus, our findings differ from those for fast room-temperature water dynamics at soft surfaces of micelles, which were largely independent of the chemical nature of the interface.[10] On the other hand, the motion of liquid water in the starting material merely modified by APTES linkers hardly differs from that in the native counterparts. As for the crystalline water fractions, we found that the dynamics are very similar in all studied confinements but much faster than those of hexagonal or cubic ice in the bulk, implying distorted ice structures in nanoscale confinements.

The finding that Ala with the smallest residue takes an intermediate position between Lys and Glu implies that the flexibility of the surface groups is not the decisive parameter for the reorientation rates of neighboring water molecules. Rather, the observed order suggests that the rotational motion of water is slower near amino acids with basic residues than those with acidic residues. These trends relating to the surface chemistry should be further scrutinized in future work. Previous studies on amino acid solutions reported that the degree of hydrogen bonding differs for water near hydrophilic and hydrophobic residues[100] and for hydrogen-bond donor and acceptor groups.[101] However, simulation studies,[101] including amino-acid resolved water dynamics at protein surfaces,[12] reported that positively charged Lys slows down water dynamics less than negatively charged Glu, different from the present findings for amino-acid functionalized silica pores. Our result that the APTES modification hardly affects the water reorientation is consistent with the outcome of an analogous study on alike modified pores with a smaller diameter of ~2 nm in the common temperature range.[65] For APTES, it was reported that the amino groups bind to other polar surface entities, e.g., the silanol groups,[102] precluding steric hindrance for water motion and rendering the pore walls less hydrophilic and, hence, reducing water–matrix interactions.

Unlike the chemistry of the inner surfaces, the diameter of silica pores had no significant effects on the rotational motion of confined water in broad ranges of the size (2–11 nm) and temperature (140–320 K).[18,62] Partly, this independence of the confinement size can be attributed to the fact that the thickness of the nonfreezable water layer at the pore wall is largely independent of the nominal pore diameter.[13,14] At the same time, the reorientation dynamics of the interfacial water at silica surfaces was found to agree with that of bulk water[97,103] at both very weak and very strong supercooling,[21,62] where such comparison is not hampered by crystallization. Nonetheless, the translational diffusion of water in silica pores is often substantially slower than in the bulk liquid.[63,104]

Altogether, our ^{2}H NMR analyses revealed that the reorientation dynamics of supercooled confined water are strongly affected by the chemistry of the confining walls, whereas previous studies reported that they weakly depend on the size of the geometrical restriction. Both findings are plausible when we consider that partial crystallization occurs in sufficiently wide confinements, including the present ones. As a result, the liquid water is sandwiched between the pore walls and the ice core and, hence, the water molecules are in immediate contact with the surface groups, while the thickness of this interfacial layer is largely independent of the nominal pore size. We observed that the water reorientation is slowest for basic Lys, followed by neutral Ala and acidic Glu functional groups, suggesting that the surface charge and the pH value inside the interfacial layer may be relevant parameters. To test the latter speculation, we intend to measure and vary the pH value near inner pore surfaces in future work.

SUPPLEMENTARY MATERIAL

See the supplementary material for the characterization of the amino-acid functionalized silica pores using elemental analysis, thermogravimetric analysis, and nitrogen gas adsorption, additional ^{2}H NMR spectra of D_2O in the modified silica pores, the ^{2}H magnetization buildup of D_2O in SBA–ALA at 300 K, ^{2}H SLR times from spectrally resolved analyses, and the temperature-dependent stretching parameters β_1 of the liquid and crystalline water fractions in the modified silica pores.

AUTHORS' CONTRIBUTIONS

E.S. and T.W. contributed equally to this work.

ACKNOWLEDGMENTS

The authors thank the LOEWE project iNAPO funded by the Ministry of Higher Education, Research and the Arts (HMWK) of the Hessen state and the Forschungsgruppe FOR 1583 (Grant Nos. Bu-911/18-2 and Vo-905/8-2) funded by the Deutsche Forschungsgemeinschaft (DFG).

DATA AVAILABILITY

The data that support the findings of this study are available from the corresponding author upon reasonable request.

REFERENCES

[1] B. Bagchi, *Water in Biological and Chemical Processes: From Structure and Dynamics to Function* (Cambridge University Press, 2013).
[2] P. Ball, Chem. Rev. **108**, 74 (2008).
[3] H. E. Stanley, S. V. Buldyrev, G. Franzese, P. Kumar, F. Mallamace, M. G. Mazza, K. Stokely, and L. Xu, J. Phys.: Condens. Matter **22**, 284101 (2010).
[4] R. Richert, Annu. Rev. Phys. Chem. **62**, 65 (2011).
[5] G. Buntkowsky, M. Vogel, and R. Winter, Z. Phys. Chem. **232**, 937 (2018).
[6] J. Geske, M. Harrach, L. Heckmann, R. Horstmann, F. Klameth, N. Müller, E. Pafong, T. Wohlfromm, B. Drossel, and M. Vogel, Z. Phys. Chem. **232**, 1187 (2018).
[7] R. Biswas and B. Bagchi, J. Phys.: Condens. Matter **30**, 013001 (2018).
[8] A. M. Dokter, S. Woutersen, and H. J. Bakker, Proc. Natl. Acad. Sci. U. S. A. **103**, 15355 (2006).
[9] M. D. Fayer and N. E. Levinger, Annu. Rev. Anal. Chem. **3**, 89 (2010).
[10] M. D. Fayer, Acc. Chem. Res. **45**, 3 (2012).
[11] D. Laage, T. Elsaesser, and J. T. Hynes, Chem. Rev. **117**, 10694 (2017).
[12] B. Qiao, F. Jiménez-Ángeles, T. D. Nguyen, and M. Olvera de la Cruz, Proc. Natl. Acad. Sci. U. S. A. **116**, 19274 (2019).
[13] S. Kittaka, S. Ishimaru, M. Kuranishi, T. Matsuda, and T. Yamaguchi, Phys. Chem. Chem. Phys. **8**, 3223 (2006).
[14] S. Jähnert, F. Vaca Chávez, G. E. Schaumann, A. Schreiber, M. Schönhoff, and G. H. Findenegg, Phys. Chem. Chem. Phys. **10**, 6039 (2008).
[15] R. Bergman and J. Swenson, Nature **403**, 283 (2000).
[16] L. Liu, S.-H. Chen, A. Faraone, C.-W. Yen, and C.-Y. Mou, Phys. Rev. Lett. **95**, 117802 (2005).
[17] S. Cerveny, Á. Alegría, and J. Colmenero, Phys. Rev. B **77**, 031803 (2008).
[18] M. Sattig and M. Vogel, J. Phys. Chem. Lett. **5**, 174 (2014).
[19] K. H. Kim, A. Späh, H. Pathak, F. Perakis, D. Mariedahl, K. Amann-Winkel, J. A. Sellberg, J. H. Lee, S. Kim, J. Park, K. H. Nam, T. Katayama, and A. Nilsson, Science **358**, 1589 (2017).
[20] J. K. H. Fischer, P. Sippel, D. Denysenko, P. Lunkenheimer, D. Volkmer, and A. Loidl, Commun. Phys. **3**, 95 (2020).
[21] J. Swenson and S. Cerveny, J. Phys.: Condens. Matter **27**, 033102 (2015).
[22] S. Cerveny, F. Mallamace, J. Swenson, M. Vogel, and L. Xu, Chem. Rev. **116**, 7608 (2016).
[23] J. Swenson, Phys. Chem. Chem. Phys. **20**, 30095 (2018).
[24] P. H. Poole, F. Sciortino, U. Essmann, and H. E. Stanley, Nature **360**, 324 (1992).
[25] P. G. Debenedetti, J. Phys.: Condens. Matter **15**, R1669 (2003).
[26] J. A. Rupley and G. Careri, Adv. Protein Chem. **41**, 37 (1991).
[27] P. W. Fenimore, H. Frauenfelder, B. H. McMahon, and R. D. Young, Proc. Natl. Acad. Sci. U. S. A. **101**, 14408 (2004).
[28] B. Bagchi, Chem. Rev. **105**, 3197 (2005).
[29] S. Khodadadi and A. P. Sokolov, Soft Matter **11**, 4984 (2015).
[30] M.-C. Bellissent-Funel, A. Hassanali, M. Havenith, R. Henchman, P. Pohl, F. Sterpone, D. van der Spoel, Y. Xu, and A. E. Garcia, Chem. Rev. **116**, 7673 (2016).
[31] Y. Qin, M. Jia, J. Yang, D. Wang, L. Wang, J. Xu, and D. Zhong, J. Phys. Chem. Lett. **7**, 4171 (2016).
[32] S.-H. Chen, L. Liu, E. Fratini, P. Baglioni, A. Faraone, and E. Mamontov, Proc. Natl. Acad. Sci. U. S. A. **103**, 9012 (2006).
[33] S. Khodadadi, S. Pawlus, and A. P. Sokolov, J. Phys. Chem. B **112**, 14273 (2008).
[34] W. Doster, S. Busch, A. M. Gaspar, M. S. Appavou, J. Wuttke, and H. Scheer, Phys. Rev. Lett. **104**, 098101 (2010).
[35] K. Kämpf, D. Demuth, M. Zamponi, J. Wuttke, and M. Vogel, J. Chem. Phys. **152**, 245101 (2020).
[36] J. Swenson, H. Jansson, and R. Bergman, Phys. Rev. Lett. **96**, 247802 (2006).
[37] C. Gainaru, A. Fillmer, and R. Böhmer, J. Phys. Chem. B **113**, 12628 (2009).
[38] A. Panagopoulou, A. Kyritsis, N. Shinyashiki, and P. Pissis, J. Phys. Chem. B **116**, 4593 (2012).
[39] S. Capaccioli, K. L. Ngai, S. Ancherbak, M. Bertoldo, G. Ciampalini, M. S. Thayyil, and L.-M. Wang, J. Chem. Phys. **151**, 034504 (2019).
[40] M. Nakanishi and A. P. Sokolov, J. Non-Cryst. Solids **407**, 478 (2015).
[41] K. Sasaki, I. Popov, and Y. Feldman, J. Chem. Phys. **150**, 204504 (2019).
[42] H. Peemoeller, F. G. Yeomans, D. W. Kydon, and A. R. Sharp, Biophys. J. **49**, 943 (1986).
[43] F. Mallamace, S.-H. Chen, M. Broccio, C. Corsaro, V. Crupi, D. Majolino, V. Venuti, P. Baglioni, E. Fratini, C. Vannucci, and H. E. Stanley, J. Chem. Phys. **127**, 045104 (2007).
[44] M. Vogel, Phys. Rev. Lett. **101**, 225701 (2008).
[45] M. Rosenstihl and M. Vogel, J. Chem. Phys. **135**, 164503 (2011).
[46] C. Mattea, J. Qvist, and B. Halle, Biophys. J. **95**, 2951 (2008).
[47] M. Tarek and D. J. Tobias, Phys. Rev. Lett. **88**, 138101 (2002).
[48] P. Kumar, Z. Yan, L. Xu, M. G. Mazza, S. V. Buldyrev, S.-H. Chen, S. Sastry, and H. E. Stanley, Phys. Rev. Lett. **97**, 177802 (2006).
[49] M. Vogel, J. Phys. Chem. B **113**, 9386 (2009).
[50] M. Heyden, J. Phys. Chem. **150**, 094701 (2019).
[51] S. Cerveny, I. Combarro-Palacios, and J. Swenson, J. Phys. Chem. Lett. **7**, 4093 (2016).
[52] M. Weigler, I. Combarro-Palacios, S. Cerveny, and M. Vogel, J. Chem. Phys. **152**, 234503 (2020).
[53] B. Grünberg, T. Emmler, E. Gedat, I. Shenderovich, G. H. Findenegg, H.-H. Limbach, and G. Buntkowsky, Chem. - Eur. J. **10**, 5689 (2004).
[54] F. Mallamace, M. Broccio, C. Corsaro, A. Faraone, U. Wanderlingh, L. Liu, C.-Y. Mou, and S. H. Chen, J. Chem. Phys. **124**, 161102 (2006).
[55] M. Rosenstihl, K. Kämpf, F. Klameth, M. Sattig, and M. Vogel, J. Non-Cryst. Solids **407**, 449 (2015).
[56] G. Buntkowsky and M. Vogel, Molecules **25**, 3311 (2020).
[57] A. Faraone, L. Liu, C.-Y. Mou, C.-W. Yen, and S.-H. Chen, J. Chem. Phys. **121**, 10843 (2004).

[58]K. Yoshida, T. Yamaguchi, S. Kittaka, M.-C. Bellissent-Funel, and P. Fouquet, J. Chem. Phys. **129**, 054702 (2008).
[59]N. Pérez-Hernández, T. Q. Luong, M. Febles, C. Marco, H.-H. Limbach, M. Havenith, C. Pérez, M. V. Roux, R. Pérez, and J. D. Martín, J. Phys. Chem. C **116**, 9616 (2012).
[60]A. Vyalikh, T. Emmler, B. Grünberg, Y. Xu, I. Shenderovich, G. H. Findenegg, H.-H. Limbach, and G. Buntkowsky, Z. Phys. Chem. **221**, 155 (2007).
[61]J. Sjöström, J. Swenson, R. Bergman, and S. Kittaka, J. Chem. Phys. **128**, 154503 (2008).
[62]M. Weigler, M. Brodrecht, G. Buntkowsky, and M. Vogel, J. Phys. Chem. B **123**, 2123 (2019).
[63]M. Weigler, E. Winter, B. Kresse, M. Brodrecht, G. Buntkowsky, and M. Vogel, Phys. Chem. Chem. Phys. **22**, 13989 (2020).
[64]S. A. Yamada, S. T. Hung, W. H. Thompson, and M. D. Fayer, J. Chem. Phys. **152**, 154704 (2020).
[65]M. Weigler, M. Brodrecht, H. Breitzke, F. Dietrich, M. Sattig, G. Buntkowsky, and M. Vogel, Z. Phys. Chem. **232**, 1041 (2018).
[66]J. Deschamps, F. Audonnet, N. Brodie-Linder, M. Schoeffel, and C. Alba-Simionesco, Phys. Chem. Chem. Phys. **12**, 1440 (2010).
[67]S. Jayanthi, S. Kababya, A. Schmidt, and S. Vega, J. Phys. Chem. C **120**, 2797 (2016).
[68]S. Jayanthi, M. Werner, Y. Xu, G. Buntkowsky, and S. Vega, J. Phys. Chem. C **117**, 13114 (2013).
[69]X. Wang, K. S. K. Lin, J. C. C. Chan, and S. Cheng, J. Phys. Chem. B **109**, 1763 (2005).
[70]P. Yang, S. Gai, and J. Lin, Chem. Soc. Rev. **41**, 3679 (2012).
[71]M. Vogel, Eur. Phys. J.: Spec. Top. **189**, 47 (2010).
[72]M. Sattig, S. Reutter, F. Fujara, M. Werner, G. Buntkowsky, and M. Vogel, Phys. Chem. Chem. Phys. **16**, 19229 (2014).
[73]M. Sattig, K. Elamin, M. Reuhl, J. Swenson, and M. Vogel, J. Phys. Chem. C **121**, 6796 (2017).
[74]S. A. Lusceac, M. R. Vogel, and C. R. Herbers, Biochim. Biophys. Acta, Proteins Proteomics **1804**, 41 (2010).
[75]S. A. Lusceac and M. Vogel, J. Phys. Chem. B **114**, 10209 (2010).
[76]S. A. Lusceac, M. Rosenstihl, M. Vogel, C. Gainaru, A. Fillmer, and R. Böhmer, J. Non-Cryst. Solids **357**, 655 (2011).
[77]M. Brodrecht, H. Breitzke, T. Gutmann, and G. Buntkowsky, Chem. - Eur. J. **24**, 17814 (2018).
[78]S. Schneider, C. Säckel, M. Brodrecht, H. Breitzke, G. Buntkowsky, and M. Vogel, J. Chem. Phys. **153**, 244501 (2020).
[79]In Ref. 78, the starting material was denoted as SBA-15A.
[80]C. Yue, J. Thierry, and P. Potier, Tetrahedron Lett. **34**, 323 (1993).
[81]W. Tegge, W. Bautsch, and R. Frank, J. Pept. Sci. **13**, 693 (2007).
[82]M. J. Schöwe, O. Keiper, C. Unverzagt, and V. Wittmann, Chem. - Eur. J. **25**, 15759 (2019).
[83]E. P. Barrett, L. G. Joyner, and P. P. Halenda, J. Am. Chem. Soc. **73**, 373 (1951).
[84]P. I. Ravikovitch and A. V. Neimark, J. Phys. Chem. B **105**, 6817 (2001).
[85]K. Schmidt-Rohr and H.-W. Spiess, *Multidimensional Solid-State NMR and Polymers* (Academic Press, 1994).
[86]A. Abragam, *Principles of Nuclear Magnetism*, 2nd ed. (Oxford University Press, 1983).
[87]N. Bloembergen, E. M. Purcell, and R. V. Pound, Phys. Rev. **73**, 679 (1948).
[88]R. Böhmer, G. Diezemann, G. Hinze, and E. Rössler, Prog. Nucl. Magn. Reson. Spectrosc. **39**, 191 (2001).
[89]H. W. Spiess and H. Sillescu, J. Magn. Reson. **42**, 381 (1981).
[90]C. Schmidt, K. J. Kuhn, and H.-W. Spiess, Prog. Colloid Polym. Sci. **71**, 71 (1985).
[91]M. Brodrecht, E. Klotz, C. Lederle, H. Breitzke, B. Stühn, M. Vogel, and G. Buntkowsky, Z. Phys. Chem. **232**, 1003 (2018).
[92]Q. Z. Ni, E. Markhasin, T. V. Can, B. Corzilius, K. O. Tan, A. B. Barnes, E. Daviso, Y. Su, J. Herzfeld, and R. G. Griffin, J. Phys. Chem. B **121**, 4997 (2017).
[93]A. Esadze, D.-W. Li, T. Wang, R. Brüschweiler, and J. Iwahara, J. Am. Chem. Soc. **133**, 909 (2011).
[94]C. Lederle, M. Sattig, and M. Vogel, J. Phys. Chem. C **122**, 15427 (2018).
[95]F. Löw, K. Amann-Winkel, T. Loerting, F. Fujara, and B. Geil, Phys. Chem. Chem. Phys. **15**, 9308 (2013).
[96]B. Geil, T. M. Kirschgen, and F. Fujara, Phys. Rev. B **72**, 014304 (2005).
[97]J. Qvist, C. Mattea, E. P. Sunde, and B. Halle, J. Chem. Phys. **136**, 204505 (2012).
[98]S. Cerveny and J. Swenson, Phys. Chem. Chem. Phys. **16**, 22382 (2014).
[99]D. E. Woessner, J. Chem. Phys. **35**, 41 (1961).
[100]M. Ide, Y. Maeda, and H. Kitano, J. Phys. Chem. B **101**, 7022 (1997).
[101]F. Sterpone, G. Stirnemann, J. T. Hynes, and D. Laage, J. Phys. Chem. B **114**, 2083 (2010).
[102]A. A. Golub, A. I. Zubenko, and B. V. Zhmud, J. Colloid Interface Sci. **179**, 482 (1996).
[103]S. Lemke, P. H. Handle, L. J. Plaga, J. N. Stern, M. Seidl, V. Fuentes-Landete, K. Amann-Winkel, K. W. Köster, C. Gainaru, T. Loerting, and R. Böhmer, J. Chem. Phys. **147**, 034506 (2017).
[104]F. Stallmach, J. Kärger, C. Krause, M. Jeschke, and U. Oberhagemann, J. Am. Chem. Soc. **122**, 9237 (2000).